Paper

Influence of Initial Extruded Microstructures of Al-4.4Zn-1.4Mg Alloy Flat Bar on VDA Bendability*

Amalina Aina Kaharudin**, Ran Saeki***, Mai Takaya****,
Tadashi Minoda***** and Tomoyuki Homma******

The bendability of extruded Al-4.4Zn-1.4Mg (mass%) alloy flat bars with 1.4 mm thickness having two types of microstructures which are fibrous and recrystallized is evaluated by a Verband der Automobilindustrie (VDA) bending test without pre-strain. The recrystallized specimen has better bendability than the fibrous one. The texture condition nearby the surfaces affects the VDA bendability the most. However, the microvoid formations also contribute in faster cracking phenomena during the load drop of the VDA bending test.

Keywords: *Verband der Automobilindustrie, 7000 series aluminum alloy, extrusion, electron backscatter diffraction, texture*

1. Introduction

Verband der Automobilindustrie (VDA) bending test (VDA 238-100) for evaluation of bendability has been standardized by the German Association of the Automotive Industry.[1] This test was developed to evaluate local formability and resistance to cracking of automobile parts during a collision. A load-stroke graph is obtained during the VDA bending test, and a bending angle at a certain load can be calculated using VDA 238-100 standard formula.[1] The bending angle at the maximum load (α_{Fmax}) of the test is believed to initiate cracks or to be the bending limit. Nevertheless, it is commonly assumed that a material reaches its failure beyond a 30 N load drop after hitting the maximum load. Thus, the VDA bending angle (α_{-30N}) is then determined when it reaches the 30 N load drop.

Early research on the VDA is reported by Larour et al. regarding the detailed method of the test using steels.[2, 3] Naito et al. also reported on the VDA bendability of steels with microstructural observations,[4] while Cheong et al. reported on the VDA bendability of steels, aluminum and magnesium alloys with strain analyses using a digital image correlation (DIC) method.[5] The correlation between the bendability and local ductility in 5754 and 6111 aluminum alloys was evaluated with the DIC strain measurement by Kupke et al., and they found that crack initiation occurs at the center of the samples, and it propagates towards a sample edge.[6] Noder et al. applied pre-strain to promote cracking for the subsequent bending test and then observed with DIC "hairline surface cracking" on the outer surface, providing failure detection methods in a dual phase steel and 5182 aluminum and ZEK100 magnesium alloys.[7, 8] Panich and Kalawong compared the Nakajima stretching and VDA bending tests with pre-strain as for forming and bending limit curves, respectively; [9] they used uniaxial tensile, hydraulic bulge and disk compression tests to investigate the bending limit stress curves for a high strength steel.

Although these experiments were concerned about the importance of an outer layer, effects of microstructures on such outermost layers as well as internal microstructure in the VDA bendability have never been discussed.

The use of 7000 series aluminum alloys in automobiles is still smaller in amount than that of the 5000 and 6000 series alloys. However, the 7000 series alloys are still being considered as a potential replacement to contribute to lighter automobiles, thus improving fuel efficiency and catching up with the development of hybrid, electric and fuel cell vehicles. One of the commonly used 7000 series alloys is 7204 alloy, which is aimed at being used as a bumper. Therefore, the bendability of the alloy needs to be improved for safety of passengers.

By changing the homogenization temperature of an aluminum alloy, two types of microstructures, fibrous and recrystallized, can be obtained.[10] This microstructural control is enabled by addition of a small amount of transition metals such as Mn, Cr and/or Zr. If the alloy is homogenized at a low temperature after casting, fine compounds containing the transition metals are formed, and they act as pinning particles at grain boundaries to suppress recrystallization and grain growth. On the other hand, when the homogenization temperature is high, coarse precipitates are formed, and they become nucleation sites for recrystallization, which is known as particle-stimulated nucleation.[11, 12]

Controlling types of the initial extruded microstructures improves mechanical properties of the alloy. For example, Ohori et al. reported that the fibrous specimen of an extruded rod has higher tensile strength than the recrystallized one with approximately 100 MPa difference.[10] The recrystallized microstructure is, however, often said to have excellent impact resistance and bendability due to its Cube $\{001\}\langle100\rangle$ orientation texture.[13, 14] It has a lower Taylor factor than the other typical textures in aluminum, which indicates that a less stress is needed to undergo uniform slip deformations. Crystal orientations with high Taylor factors require higher stresses for the slip deformations to occur uniformly. This causes heterogeneous local deformations like shear bands to form easily.[14]

Thus, in this study, we investigate effects of microvoids that are formed due to presence of second phase particles, which form during homogenization, and shear bands formation that is mainly related to crystallographic textures to elucidate the VDA bending deformation mechanisms in the Al-4.4Zn-1.4Mg (mass%) alloy (7204-like aluminum alloy) without pre-strain. The microstructural analyses were made both on outermost layers and inner regions with respect to the normal direction because they are significantly different from each other in extruded flat bars.

2. Experimental Procedures

Table 1 shows the chemical composition of the Al-4.4Zn-1.4Mg alloy used in this study. Mn was not included in the alloy as the alloy shows higher strength and better bendability without it. The alloy was direct-chill cast into a cylindrical-shaped billet with a 90 mm diameter. Then, the samples cut from the billet were homogenized at 743 and 853 K for 8 h to achieve fibrous and recrystallized microstructures, respectively. After the homogenization, both samples were air-cooled. The extrusion was conducted at 723 K using a direct extrusion method with a ram speed of 1.3 mm/s and an extrusion ratio of 66 to produce flat bars with a cross section of a 70 mm width and a 1.5 mm thickness, which were then air-cooled. After that, the extrudates were solution treated at 743 K for 1 h, followed by water quenching. Finally, artificial aging was conducted at 393 K for 24 h, followed by air cooling to achieve the peak hardness. The VDA bending angle was measured following VDA 238-100 standards using in-house-made jigs which were installed to a universal testing machine (INSTRON 3369). **Table 2** shows the VDA bending test conditions. **Fig. 1** shows the schematic diagram of the VDA bending test set-up where the load direction is parallel to normal direction (ND). The ED and TD in Fig. 1 stand for the extrusion and transverse directions of the samples, respectively.

Table 1 Chemical composition of the aluminum alloy used in this study (mass%).

Si	Mg	Fe	Zr	Zn	Ti	Al
0.02	1.4	0.13	0.14	4.4	0.01	bal.

Table 2 VDA bending test conditions.

Parameter	Value
Sample thickness, a	1.4 mm
Sample width, b	30 mm
Sample length, l	60 mm
Punch radius	0.2 mm
Punch depth	10 mm
Punch width	2 mm
Rollers diameter, D	30 mm
Clearance between rollers, L	2.8 mm
Initial load, F	30 N
Test velocity	0.3 mm/s

Fig. 1 VDA bending test set-up.

α_{Fmax} was calculated using a stroke value of the maximum load while α_{-30N} was calculated using the stroke value when the load dropped 30 N after reaching the maximum load. Both the angles were calculated using the VDA 238-100 standard equations.[1), 5)]

Finite element method (FEM) analyses were conducted using design environment for forming (Scientific Forming Technologies Corporation DEFORM ver. 12). All conditions were corresponding to values given in Table 2. Even though rollers rotated automatically when the loads were applied to a flat bar, it was essential to assume that friction between the rollers and sample still occurred due to a contact. Thus, the friction coefficient between the rollers and sample was set to 0.82 here, which was a general friction coefficient value between aluminum alloys and steels.[15)] In addition, we used nominal stress-strain curves from tensile tests obtained from both the samples having fibrous and recrystallized microstructures as the material data. However, bear in mind that the grain sizes and textures were not accounted in these analyses.

Microstructural observations were mainly conducted using a scanning electron microscope (SEM) as it was hard to distinguish between coarse grains at surface areas and grains of inner microstructure of the recrystallized samples. The SEM equipment used was a field emission scanning electron microscope (FESEM, Hitachi SU8230) which was equipped with a cold field emission gun and an electron backscatter diffraction (EBSD) detector (Oxford Instruments NordlysNano). The SEM observations were operated at 15 kV on ND-TD planes. The EBSD data were obtained using step sizes of 1 and 2 μm for unbent and bent samples,
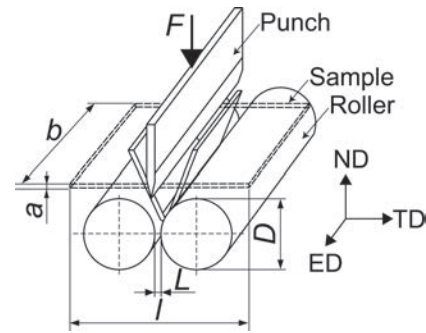
respectively. Band contrast (BC) images, inverse pole figure (IPF) maps, pole figures (PFs) and local misorientation (LM) images were produced from the EBSD data with software (Oxford Instrument AztecHKL CHANNEL5). Crystallite orientation distribution function (ODF) was obtained using TSL OIM analysis software by converting data obtained by the NordlysNano detector to the format for TSL. The ODF results were then further converted into three-dimensional skeleton lines which was constructed in software (Kitware Inc., Sandia National and Los Alamos National Laboratories ParaView ver. 5.9.0).

Another SEM (Hitachi Flex-SEM 1000 II) was used to quantitatively evaluate size and volume fraction of second phase particles and to observe shear bands and microvoids formed at α_{Fmax} through back-scattered electron (BSE) images. Both fibrous and recrystallized samples were etched using Keller's reagent which consists of 2 ml HF, 5 ml HNO_3, 3 ml HCl and 190 ml distilled water. In order to observe the shear bands in bent samples, they were artificially aged again at 393 K for 24 h to allow precipitation on dislocations. The precipitation made the shear bands more visible after etching. The observations were operated at 15 kV on ND-TD planes.

Lastly, an optical microscope (OM, Nikon Eclipse LV150N) was also used to observe the shear bands and cracks after the VDA bending tests.

3. Results and Discussion

Fig. 2 shows load-stroke curves taken during VDA bending tests of fibrous and recrystallized specimens done with 3 test samples each. **Fig. 3** summarizes the α_{Fmax} and α_{-30N} values measured referring the load-

stroke curves shown in Fig. 2. The recrystallized specimen has larger α_{Fmax} and α_{-30N} than the fibrous one with roughly 30 and 40° differences, respectively. The differences in bending angle between α_{Fmax} and α_{-30N} for the fibrous and recrystallized specimens are 5 and 20°, respectively, which indicates that the fibrous specimen undergoes cracking faster than the recrystallized one.[16]

In order to understand the bending deformation mechanism of the VDA bending test, FEM analyses were conducted using nominal stress-strain data obtained at ambient temperature for each sample. **Fig. 4** shows the maximum shear stress states of fibrous and recrystallized specimens at their respective α_{Fmax}; the bending angle is set to 57 and 97°, respectively. The fibrous specimen which has smaller α_{Fmax} than the recrystallized one experiences higher maximum shear stress at the range of 205～220 MPa near the surfaces on the ED-TD plane. The depth of the high maximum shear stress area at the
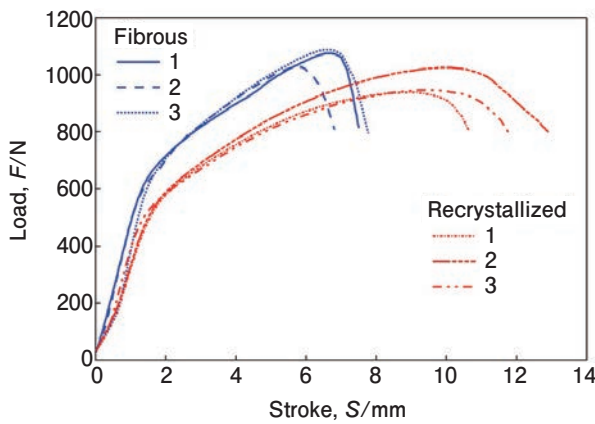

Fig. 2 Load-stroke curves of fibrous and recrystallized specimens during VDA bending.
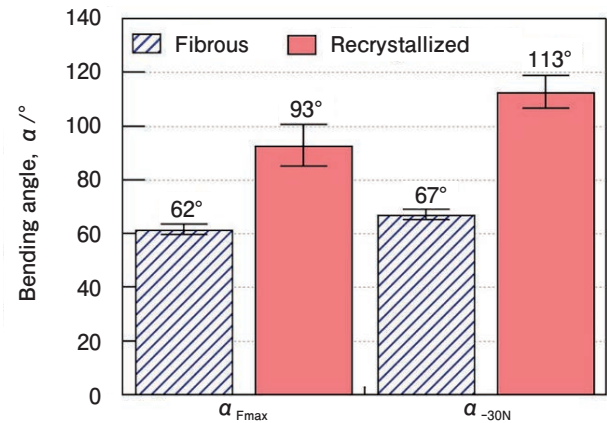

Fig. 3 α_{Fmax} and α_{-30N} of fibrous and recrystallized specimens calculated from load-stroke curves in Fig. 2.
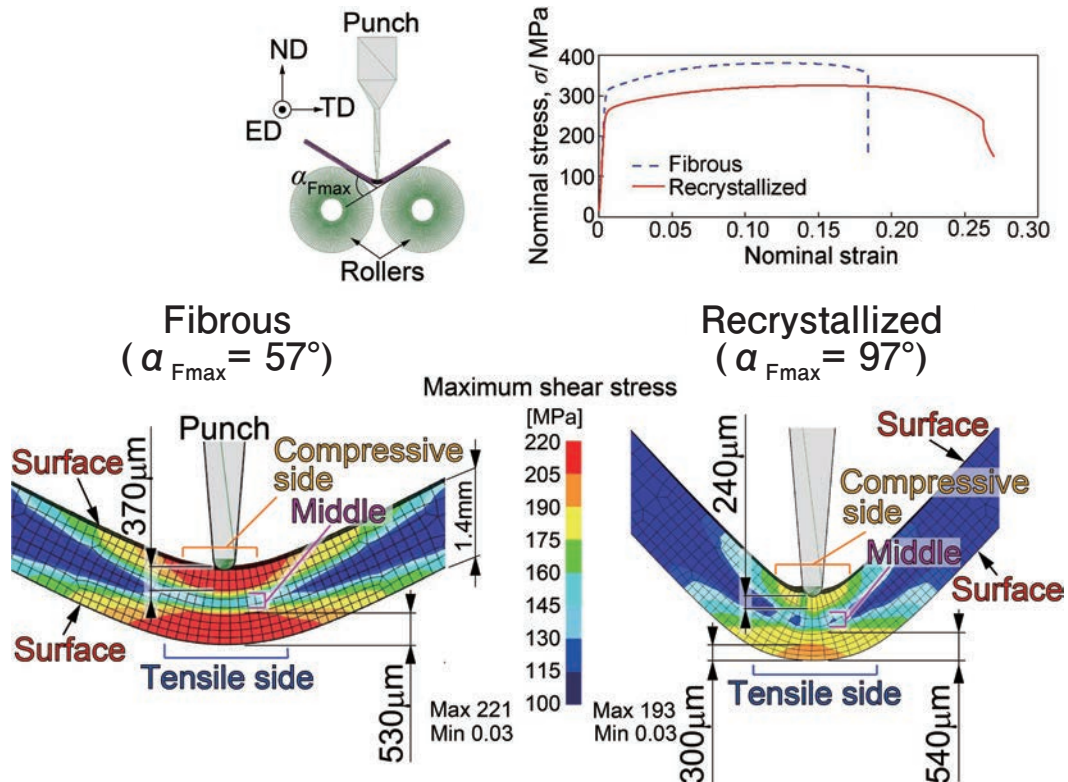

Fig. 4 Maximum shear stress distribution from FEM analyses in fibrous and recrystallized specimens at α_{Fmax}. The definition of the bending angle and the nominal stress vs. nominal strain curves of the two specimens used for FEM analyses are indicated on the top of the figure.

compressive side is approximately 370 μm while at the tensile side is 530 μm. The difference in the maximum shear stress between the outermost surfaces and middle area in between both sides is about 75 MPa. The recrystallized specimen also possesses qualitatively the same maximum shear stress states like the fibrous one. However, the highest maximum shear stress is only up to 193 MPa, and the area with orange color scale (190～205 MPa) is only about 300 μm depth from the tensile outermost surface. The yellow color scale areas with the maximum shear stresses ranging from 170 to 195 MPa are approximately 240 μm at the compressive side and 540 μm at the tensile side. It is thus clear that the areas near the surfaces experience high maximum shear stresses than the middle parts. These results are well corresponding to the previous reports.[5]～[7] Although the high maximum shear stress depth might differ depending on a type of a material or microstructure, it does not change the fact that the surface areas are the most affected during the VDA bending deformation.

Fig. 5 shows IPF map and PF acquired from ND-TD planes of the extrudates without bending to understand effects of texture on the bendability of both the microstructures. The average grain sizes in diameter (d_{ave}) measured using an equivalent circular area diameter method are also indicated in Fig. 5. The fibrous microstructure possesses significantly small grain sizes due to a pinning effect of second phase particles with transition metals during extrusion.[11] Both the microstructures have coarse recrystallized grains at the surface area due to generated heat and shear strains caused by shear deformations related to metal flows during the extrusion.[17] Depths measured towards ND of the coarse grains at the surface area in both specimens are almost the same, which are about 60～90 μm. The PFs were obtained from the inner microstructure only, which meant the coarse grains were not included. The fibrous microstructure obtained high intensities from {321}, {231} and {133} planes. This PF is similar to the rolling texture reported in general aluminum alloys proposed by Wasserman when rotated to the ED-TD plane.[18] In contrast, the recrystallized microstructure significantly possesses a high intensity of the Cube texture.

Further texture confirmations in the initial state were analyzed using ODF data. Fig. 6 shows ODFs and major orientations represented in the first subspace of the three-dimensional Euler angle space (skeleton lines) of the two samples prior to bending.
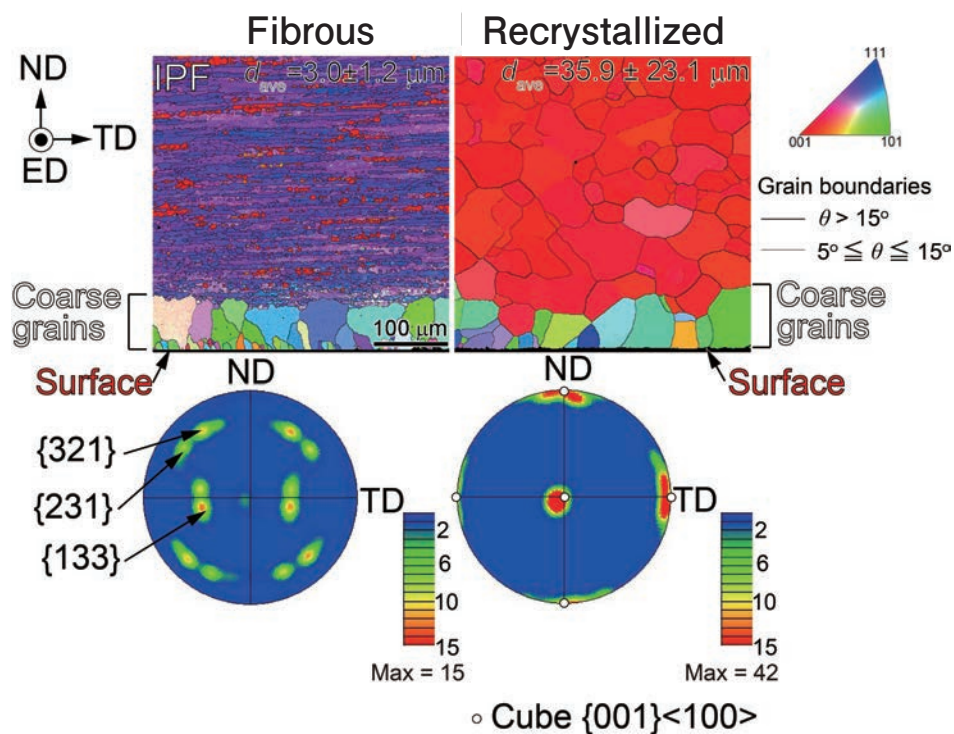

Fig. 5 IPF and (100) PF of fibrous and recrystallized microstructures from inner microstructure of initial state.
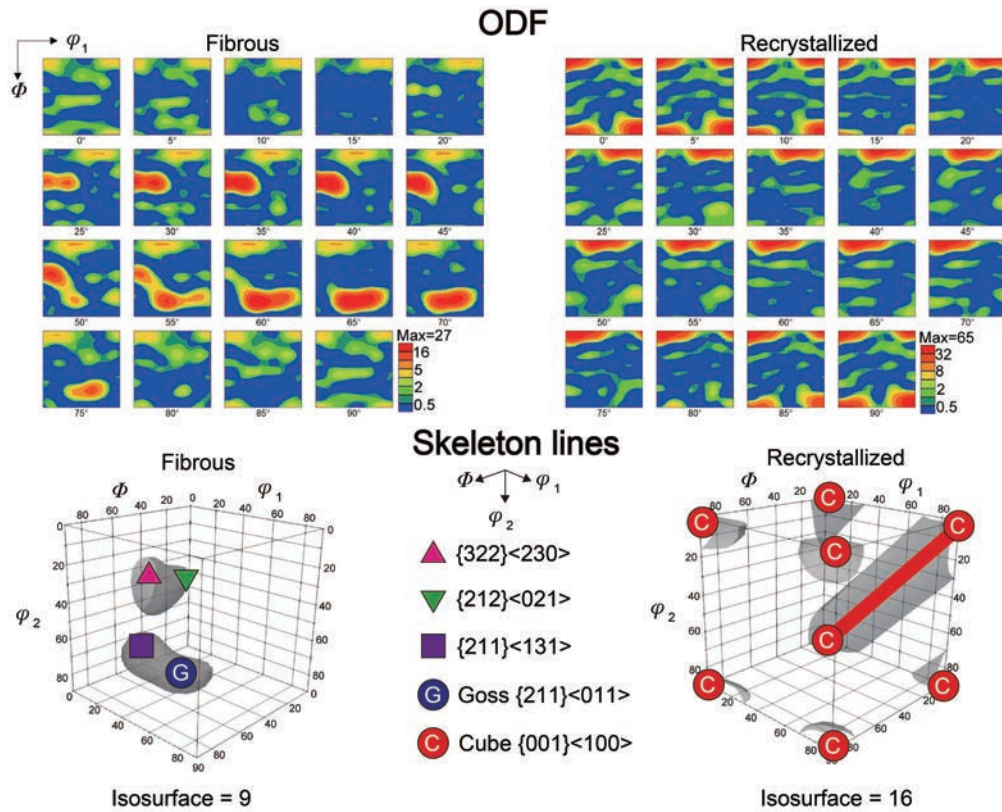
Fig. 6 ODFs and major orientations represented in the first subspace of the three-dimensional Euler angle space (skeleton lines) of the two samples prior to bending.

The skeleton lines only show textures that are the same or higher than the orange color scale in ODF; the isosurface values for each sample are given in Fig. 6. The fibrous microstructure possesses orientation distributions of {322}⟨230⟩ to {212}⟨021⟩ and {211}⟨131⟩ to Goss {211}⟨011⟩. On the other hand, the recrystallized microstructure reveals the strong Cube texture.

Fig. 7 shows the BC and LM images, IPF maps and PFs of fibrous and recrystallized microstructures at α_{Fmax}. Shear bands (white arrows) are observed within the coarse grains observed near the surface areas and inner microstructures. LM values between 1 and 2.5° can be confirmed in those areas. It is hard to observe the shear bands in the inner microstructure due to significantly fine grain sizes of the fibrous microstructure. However, the LM image reveals that the local strains are accumulated all over the observed area. Nonetheless, the low LM concentration in certain coarse grains of the surface area could be interpreted as grains that have high Taylor factor, which means they require higher stress for the slip deformation to occur uniformly and

lead to a heterogeneous local deformation like shear band during the VDA bending deformation up to α_{Fmax}.[14] The PF of the fibrous specimen shows the assemblage of crystal orientations towards Brass {110} ⟨112⟩ during bending up to α_{Fmax}. The texture is similar to that of extruded rods of aluminum alloys, which have strong ideal rolling Brass and weak Cube textures when the PF is obtained perpendicular to the extrusion direction.[19] This could be the cause of a faster load drop until $\alpha_{\text{-30N}}$ as the Brass orientation contributes to faster shear bands formation in the fibrous microstructure.[14]

On the other hand, shear bands and slip lines can be observed clearly in the recrystallized microstructure as given in Fig. 7. The amount of shear bands and slip lines decreases after about 300 μm from the outermost surface: the LM image also shows less strain accumulations in that region. These results are well consistent with the FEM analyses shown in Fig. 4. Although the recrystallized specimen has smaller maximum shear stress at α_{Fmax} than the fibrous one, the shear strain is far smaller in the fibrous structure because of the far smaller α_{Fmax},
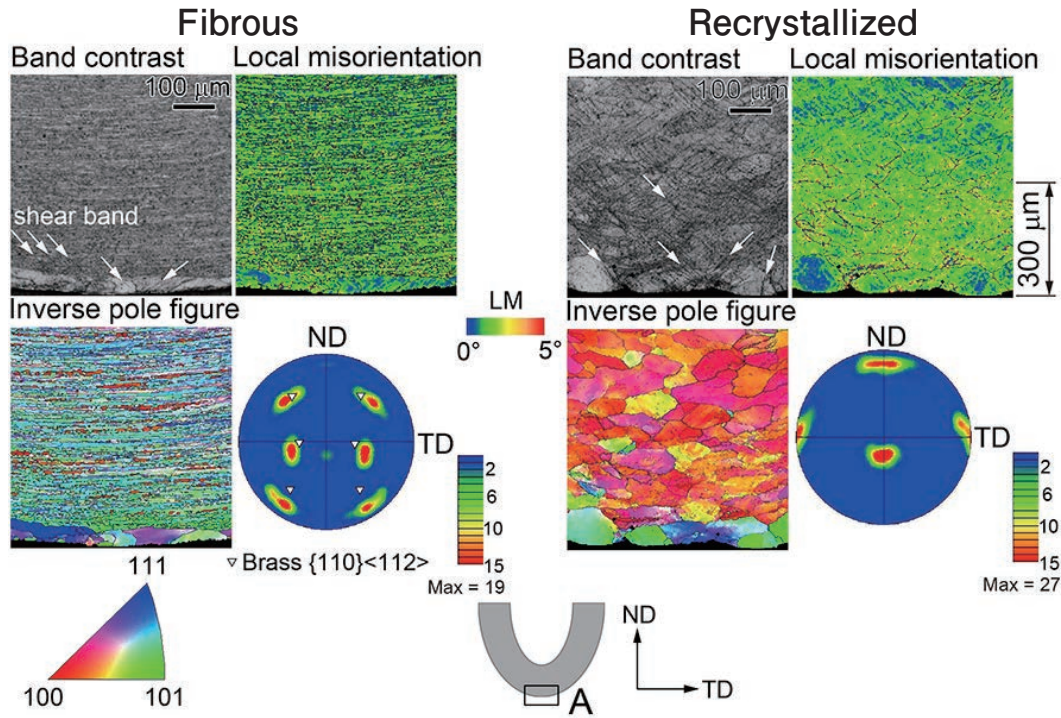
Fig. 7 BC and LM images, IPF maps and (100) PFs of both samples at α_{Fmax} and tensile sides. The observation was performed at region A.

which causes this difference in the tendency for the shear band formation in Fig. 7. Moreover, the orientation pattern does not significantly change from the Cube texture (see Fig. 5).

Yamamoto et al. reported that crack initiation and propagation during a hemming bending deformation are related to microvoid formations from existing second phase particles and shear band formations,[20] while Ashby indeed proposed that the critical size (diameter) for the microvoid formation is larger than 1 μm when we have an equiaxed second phase particle (though plate-like particles are often been shown to fracture).[21] In order to investigate this factor on the VDA bending deformation, we conducted quantitative analyses of the second phase particles within the coarse grains of the outermost surface area and the inner microstructure for both samples on BSE images. As indicated in **Fig. 8**, the coarse grains of the surface area and inner microstructure are abbreviated as "Surface" and "Interior", respectively. The second phase particles in both structures are equiaxed and plate-like shaped. **Fig. 9** provides the average diameter ($\bar{d}$) and volume fraction (V_f) of the second phase particles in fibrous and recrystallized microstructure extrudates as

indicated in Fig. 8. The average diameter $\bar{d}$ was calculated with the equivalent circular area diameter method by measuring area (A) of each particle, and then averaged them as indicated in equation (1).

$$\bar{d} = \left(\sum_{i=1}^{n} 2\sqrt{A/\pi}\right)/n \qquad (1)$$

Here, i is the index of summation and n is the total number of particles in the measured observation areas. The recrystallized microstructure owns larger diameters of the second phase particles in both the surface and interior areas. However, the fibrous microstructure has higher V_f of the second phase particles in both the areas. We observed microvoid formations at the compressive and tensile sides at α_{Fmax} using BSE images: the samples were etched to observe shear bands simultaneously. In **Fig. 10**, black and white arrows indicate shear bands and microvoids, respectively. The shear bands can be observed clearly at the tensile and compressive sides of both specimens, but the recrystallized structure possesses more shear bands than the fibrous one at the compressive side. We believe that this happens due to the sharp radius of the used punch, and the fact that the recrystallized specimen undergoes a
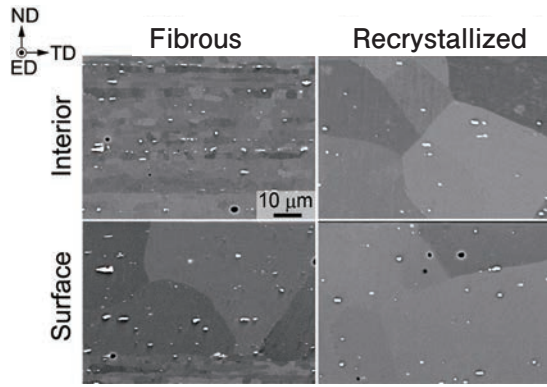
Fig. 8 BSE images of fibrous and recrystallized microstructure extrudates at the coarse grains of the surface area and the inner microstructure.
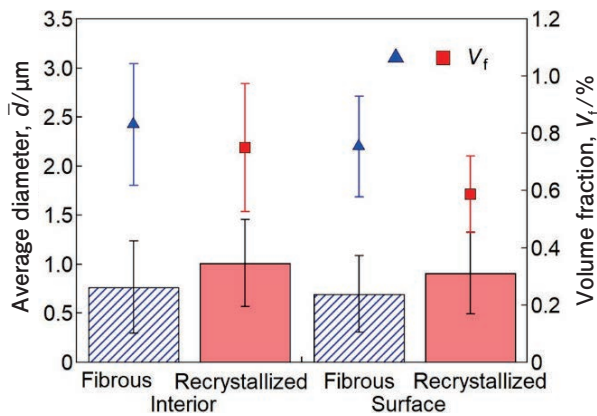

Fig. 10 BSE images of fibrous and recrystallized microstructures at α_{Fmax} (indicated in the parentheses), compressive and tensile sides.

Fig. 9 Average diameter ($\bar{d}$) and volume fraction (V_f) of second phase particles in fibrous and recrystallized microstructure extrudates.

Fig. 11 Area fraction of microvoids at tensile side and V_f of second phase particles near surfaces.

larger bending angle than the fibrous one; the grains are forcibly compressed to the loading direction of the punch. Since neither sample experiences cracking at α_{Fmax}, this point can be used to estimate the bending limit.

However, large microvoids are mainly observed in fibrous microstructure at the tensile side (both surface and interior), even though the average diameters of the second phase particles are less than 1 μm (Fig. 9). As shown in **Fig. 11**, the measured area fractions of the microvoid in the fibrous and recrystallized microstructures are 0.25 and 0.19%, respectively, while the measured volume fractions of the second phase particles in the fibrous and recrystallized microstructures are 0.76 and 0.59%, respectively; they are obtained at the tensile side and α_{Fmax}. Tendencies of increase or decrease of both the quantitative results are well consistent even though the fibrous structure possesses fewer second phase particles with diameter larger than 1 μm. Microvoids
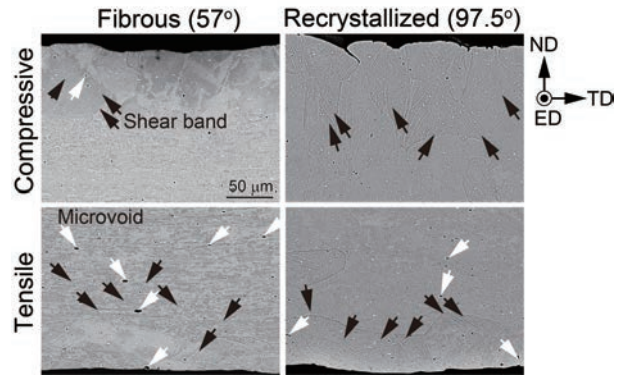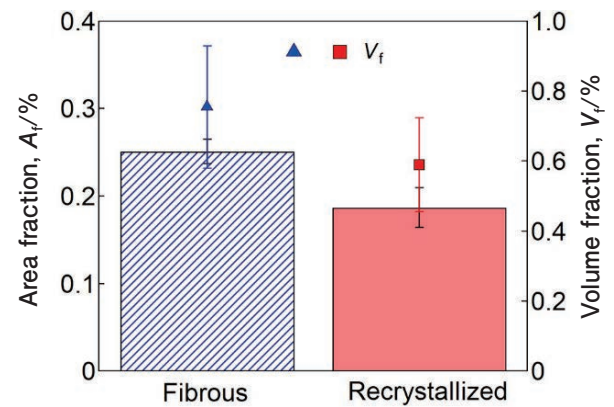
formation phenomenon does not correlate with Ashby's critical particle diameter theory due to the mixing of both equiaxed and plate-like particles. Thus, as the volume fraction of the second phase particles increases in the fibrous and tensile surface, the formation of microvoids is stimulated, leading to the faster crack formation during the load drop. The developed microvoids are exposed to the outermost surface with increasing degree of bending; as a result, they could contribute to the starting points of crack formations.[20]

Fig. 12 shows the BC images of fibrous and recrystallized microstructures at α_{-30N} and tensile sides. There is a small crack (white arrow) on the surface of the recrystallized microstructure. Shear band accumulations can be seen from the outermost surface until about a 300 μm depth in both the samples. However, the patterns of shear band accumulations are different: the shear bands tend to accumulate more at the same position in the fibrous
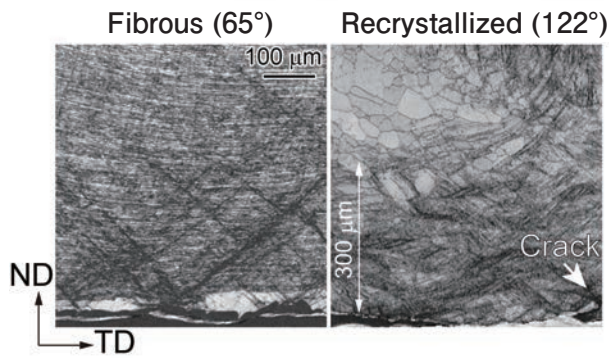
Fig. 12 BC images of fibrous and recrystallized microstructures at α_{-30N} (indicated in the parentheses).

Fig. 13 OM images of fibrous microstructure at α_{-30N} (65 °) and tensile sides with different magnifications.

microstructure, which is believed as the localized positions for the shear strain during the VDA bending. In contrast, the recrystallized microstructure displays relatively uniform shear band accumulations from the outermost surface until a 300 μm depth. This means that although the shear bands do form even in grains having the Cube texture, the tendency to accumulate on the same localized shear strain is prevented and large crack formations can be avoided, resulting in the large VDA bending angle (Fig. 3). Even though there is no crack on the fibrous microstructure in Fig. 12, we confirm presence of cracks at different areas **(Fig. 13)**, but still in the same sample. The crack is about a 300 μm long. At the tip of the crack, we can sometimes see that the crack is connected by small microvoids (dotted circle). There are two scenarios: either an array of microvoids forms and initiates a crack, which then spreads along the microvoids, or a crack forms and spreads along the shear band, after which microvoids form in front of the crack tip.

4. Conclusions

We investigated the factors that affect bendability during VDA bending deformations of the extruded Al-4.4Zn-1.4Mg alloy flat bars having fibrous and recrystallized microstructures without pre-strain. The following conclusions were obtained.

The recrystallized specimen has excellent bendability than the fibrous one. In addition, bending angle increment after α_{Fmax} is larger in the recrystallized specimen; the crack formation and propagation are slower than those in the fibrous one.
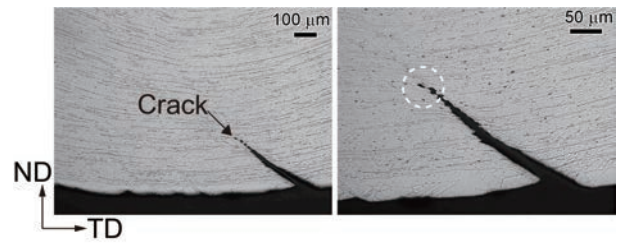
FEM analyses revealed that both the specimens experience high maximum shear stress at α_{Fmax} about $300 \sim 500$ μm depth from the outermost surface at the tensile side. In the initial state, the fibrous microstructure crystal orientation distributions of {322} ⟨230⟩ to {212} ⟨021⟩ and {211} ⟨131⟩ to Goss are predominant, whereas the recrystallized microstructure reveals strong Cube texture in inner microstructure. α_{Fmax} is proved to be a useful bending limit criterion for the extruded Al-4.4Zn-1.4Mg alloy flat bars as no cracks are observed at α_{Fmax}. Beyond α_{Fmax}, cracks about a 300 μm long is formed at the tensile side of the fibrous microstructure due to tendency of shear bands to accumulate at localized shear strain positions during the VDA bending deformation. However, in case of the recrystallized microstructure, a small crack is only observed in the coarse grains because the shear bands are well-dispersed in the area of 300 μm depth from the outermost surface, despite having a larger bending angle. Accumulation of shear bands which occurs until the 300 μm depth from the outermost surface in both the microstructures reveals that texture control and suppression of microvoids are important at this area in order to improve the bendability during the VDA bending deformation. Prevention of crack accumulations through the Cube texture existence is the most important factor in improving the VDA bendability.

Acknowledgment

REFERENCES

1) Verband der Automobilindustrie e. V., VDA 238-100 test specification, 2010.

2) P. Larour, B. Hackl, F. Leomann and K. Benedyk: IDDRG2012 conf proc., Mumbai, India (2012), 203-215.

3) P. Larour, B. Hackl and F. Leomann: IDDRG2013 conf proc., Zurich, Switzerland, (2013), 317-322.

4) J. Naito, T. Murakami and S. Otani: Kobe Steel Eng Rep., **66** (2017), 69-78.

5) K. Cheong, K. Oner, C. Butcher, R. George and J. Dykeman: IOP Conf Series: J Phys: Conf Series., **896** (2017), 102075.

6) A. Kupke, M Barnett, G. Luckey and M. Weiss: IOP Conf Series: Mater Sci Eng., **418** (2018) 012077.

7) J. Noder, A. Abedini and C. Butcher: Exp Mech., **60** (2020), 787-800.

8) J. Noder, J. Dykeman and C. Butcher: Exp Mech., **61** (2021), 367-394.

9) S. Panich and P. Kalawong: J Adv Mech Des Syst Manuf., **16** (2022), JAMDSM0013.

10) K. Ohori, H. Watanabe and Y. Takeuchi: J. JILM, **33** (1983), 718-728.

11) K. Ito: J. JILM, **30** (1980), 337-348.

12) F.J. Humphreys and M. Hatherly: *Recrystallization and related annealing phenomena*, second ed., Elsevier, Amsterdam, (2004), 293-304.

13) K. Ihara, T. Shikama and K. Morita: KOBELCO Technol Rev., **31** (2013), 69-75.

14) H. Takeda, A. Hibino and K. Takata: Mater. Trans., **51** (2010), 614-619.

15) The Japan Society of Mechanical Engineers: JSME mechanical engineers' handbook, (Tokyo, Japan, 2004), 28. (in Japanese)

16) M. Nakaya, S. Kanetada and M. Tsunezawa: KOBELCO Technol Rev., **38** (2020), 28-31.

17) Tomoyuki Homma, Takato Honma, D. Terada and M. Hoshino: Mater Sci Tech., **37** (2021), 785-793.

18) G. Wasserman (Translated by Y. Masuda): J. JILM, **17** (1967), 5-13.

19) E. Hirosawa: Trans Jpn Inst Met., **5** (1964), 235-238.

20) Y. Yamamoto, M. Asano, H. Yoshida, M. Kobayashi and H. Toda: J. JILM, **63** (2013), 452-457.

21) M.F. Ashby: Phil Mag., **14** (1966), 1157-1178.

Amalina Aina Kaharudin
Fundamental Research Department,
Research & Development Center,
Marketing & Technology Division,
UACJ Corporation, Dr. Eng.

Mai Takaya
Fundamental Research Department,
Research & Development Center,
Marketing & Technology Division,
UACJ Corporation

Tadashi Minoda
Fundamental Research Department,
Research & Development Center,
Marketing & Technology Division,
UACJ Corporation, Ph. D (Eng.)

Tomoyuki Homma
Department of Mechanical Engineering,
Nagaoka University of Technology, Ph. D (Eng.)